Nano-Micro Letters

e-ISSN 2150-5551
CN 31-2103/TB

ARTICLE

https://doi.org/10.1007/s40820-026-02357-8

Cite as
Nano-Micro Lett.
(2027) 19:61

Received: 20 April 2026
Accepted: 10 August 2026
© The Author(s) 2026

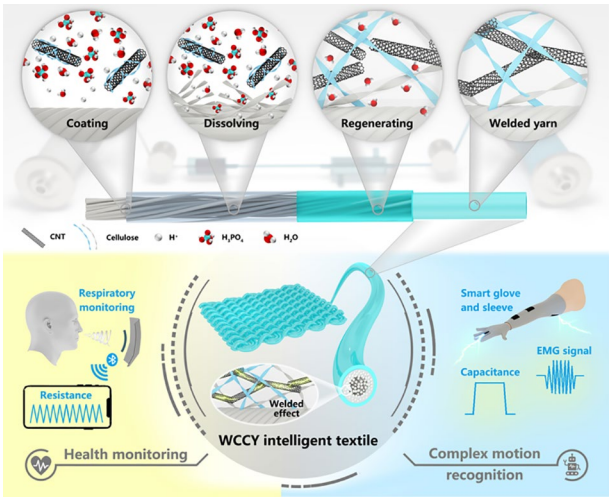
Continuous Molecular-Scale Welding of Carbon Nanotubes into Cellulose Yarns for Robust, Multisensory All-Textile Electronics

Yinqing Luo[1], Chunlin Mao[1], Yu Geng[1], Liduo Rong[1], Bijia Wang[1,2], Zhiping Mao[1,2], Xiaofeng Sui[1] ✉, Szczepan Zapotoczny[3] ✉, Xueling Feng[1,2] ✉

HIGHLIGHTS

- A continuous manufacturing strategy for robust conductive yarns is established via phosphoric acid-mediated molecular-scale welding technique.
- The synergistic effect of phosphoric acid molecular-scale welding and cellulose on the dispersion of carbon nanotubes leads to the robust dual-network topological entanglement with exceptional interfacial adhesion and washing durability.
- A single-component, multisensory all-textile platform is successfully integrated to monitor diverse biomechanical deformations, biophysical signatures, and environmental stimuli precisely and concurrently.

ABSTRACT The seamless integration of electronic functionalities into sustainable textile architectures is foundational for next-generation wearable intelligence. However, achieving high electrical performance without compromising the inherent comfort and durability of natural fibers remains a persistent challenge. Herein, we report a continuous manufacturing strategy for robust conductive yarns via phosphoric acid-mediated molecular-scale welding technique. By precisely controlling the partial dissolution and in situ regeneration of cellulose chains, carbon nanotubes (CNTs) are architecturally "locked" within the reorganized molecular framework of yarns. This structural reconfiguration establishes a highly efficient, shielded charge transport network, yielding an outstanding electrical conductivity of 334.6 S m^{-1} at an ultralow CNT loading (11.2 wt%). The resulting Welded Cellulose/CNT Yarns (WCCYs) exhibit exceptional interfacial adhesion, delivering superior mechanical tenacity and laundry durability that surpass conventional coated fibers. Leveraging these synergistic properties, we demonstrate an all-textile, multisensory platform capable of concurrent, high-fidelity monitoring of biomechanical deformations, physiological signatures, and environmental stimuli (humidity and volatile organics). The WCCY-based system enables precise respiratory pattern tracking and fine-grained recognition of hand gestures, effectively bridging the gap between molecular-level materials design and large-scale, multifunctional smart wearable applications. This work offers a scalable and sustainable route for transitioning traditional textiles into sophisticated human–machine interfaces.



KEYWORDS Molecular-scale welding; Conductive cotton yarns; Smart textiles; Multisensory electronics; Carbon nanotubes

✉ Xiaofeng Sui, suixf02@gmail.com; Szczepan Zapotoczny, s.zapotoczny@uj.edu.pl; Xueling Feng, xlfeng@dhu.edu.cn
[1] Key Lab of Sustainable Low-carbon Technologies for Textile Dyeing and Finishing, Ministry of Education, College of Chemistry and Chemical Engineering, Donghua University, Shanghai 201620, P. R. China
[2] National Innovation Center of Advanced Dyeing & Finishing Technology, Shandong Zhongkang Guochuang Research Institute of Advanced Dyeing and Finishing Technology Co., Ltd., Tai' an 271000, Shandong, P. R. China
[3] Faculty of Chemistry, Jagiellonian University, Gronostajowa 2, 30-387, Krakow, Poland

Published online: 16 November 2026

Shanghai Jiao Tong University Press

Springer

1 Introduction

Flexible electronics have received tremendous attention due to their unparalleled advantages over the conventional solid and single-shape electronic devices in personalized mobile equipment, medical healthcare systems, and human–machine interface units [1–4]. Textile-based electronic products are favored in the development of advanced wearable devices because they integrate electronic functionality with the inherent comfort of textiles [5]. As components of smart wearable systems, textile-based electronics must satisfy fundamental textile and garment requirements, including flexibility, breathability, lightweight, and robust durability [6, 7]. However, conventional conductive fabrics prepared via a top-down approach, e.g., ink coating method, tend to seal the pores of the fabric structure, compromising wearing comfort [8, 9]. In contrast, conductive fibers or yarns can be engineered from the bottom-up, enabling the construction of textiles that preserve softness, breathability, and overall wearability. Remarkably, conductive yarns can be engineered with specific functions, e.g., sensing [10, 11], energy storage [12, 13], energy harvesting [14, 15], and be used to integrate versatility in a garment through sewing, weaving, or knitting.

The field has advanced significantly through the development of multifunctional sensing fibers and yarns, which can be integrated into smart textile platforms capable of health monitoring, motion detection, and therapeutic functions [16–19]. One common strategy for fabricating fibrous sensors involves incorporating conductive functional particles into cellulosic materials [10, 12, 20, 21]. Owing to their exceptional electrical conductivity, mechanical robustness, and long-term stability, carbon nanotubes (CNTs) are perceived as an ideal candidate for constructing textile-based electronics [22, 23]. However, the hydrophobic nature and hard-to-disperse feature of CNTs continue to pose significant challenges for their practical application. Organic solvents and surfactants are commonly employed as dispersants for CNTs, but their use often raises environmental and health concerns [7, 24–26]. Therefore, there is a strong demand for the development of non-toxic, eco-friendly alternatives for CNT dispersion. Recently, cellulose has emerged as a promising dispersant due to its amphiphilic property, but the investigation of its dispersion mechanism is still not sufficient [27]. Moreover, conductive yarns coated with the aqueous CNT dispersion tend to suffer from flaking, primarily due to weak interfacial adhesion between the conductive particles and the yarn substrate [25].

Phosphoric acid, an inorganic solvent for cellulose, has been employed for its unique ability to dissolve cellulose without requiring pretreatment or co-solvents. In our prior work, we demonstrated that an 85 wt% aqueous phosphoric acid solution can efficiently dissolve cellulose and other biomass-derived materials under mild conditions, without auxiliary chemical or mechanical processes [28]. Furthermore, we proved that phosphoric acid could serve as an excellent medium for "welding" cotton yarns, by controlling partial dissolution and in situ regeneration of cellulose [29].

Thus, we hypothesize that CNT functionalization of the yarns can be conveniently achieved during the controlled partial dissolution and in situ regeneration of cellulose in the phosphoric acid welding system, leading to the spontaneous formation of a core–shell architecture. The dissolved and regenerated cellulose can serve as a binder to firmly immobilize CNTs on the yarn surface, thereby producing a robust and stable conductive yarn that addresses the delamination issue mentioned earlier.

Herein, we developed a continuous fabrication strategy for conductive yarns, wherein the in situ functionalization of CNTs on cotton yarns occurs simultaneously with the welding process (Fig. 1). Uniform CNT dispersion was achieved in aqueous phosphoric acid with the aid of pre-dissolved microcrystalline cellulose (MCC). Molecular dynamic simulations were performed to elucidate the favorable interactions between CNTs and cellulose chains. Through the facile and scalable welding technique, the functional dopes were applied to construct Welded Cellulose/CNT Yarns (WCCYs) with a core–sheath architecture, featuring a gradual transition between the dense, conductive sheath and the porous, mechanically resilient core. The immobilization and conformal coating of CNTs on the yarns were accomplished during the partial dissolution and subsequent regeneration of cellulose, ensuring robust interfacial adhesion. During treatment through the aqueous phosphoric acid, cellulose yarns undergo partial chain disentanglement, generating dynamic "docking sites" for CNTs integration. The subsequent regeneration process then "locks" the CNTs via hydrogen bond reformation and topological entanglement, facilitating in situ, binder-free functionalization with molecular-level precision and robust electrical percolation.

© The authors
https://doi.org/10.1007/s40820-026-02357-8

The conductivity, mechanical properties, wash fastness, and weavability of the WCCYs were systematically evaluated, confirming that the welding process not only reinforces the yarn structurally but also functionalizes the yarn. Remarkably, this strategy achieves an ultralow electrical percolation threshold, indicating highly efficient CNT dispersion and interfacial anchoring. Beyond performance enhancement, this in situ functionalization preserves the native yarn's structural integrity while synergistically boosting its mechanical robustness and multifunctional performance. This process eliminates the need for post-treatments or external binders, offering a green, scalable, and facile route toward next-generation smart textile manufacturing.

The WCCYs were woven into an integrated, multisensory wearable intelligent textile. This textile not only exhibits high sensitivity to environmental stimuli, such as volatile solvents and humidity variations, but also functions as a flexible, skin-conformable electrode capable of detecting both mechanical deformations and physiological electrical signal of the human body. As a proof of concept, we designed and demonstrated two functional prototypes: as a smart mask for real-time monitoring of respiratory patterns and breath biomarkers, and a smart sleeve-glove system capable of recognizing complex hand and arm gestures with high fidelity. These applications highlight the potential

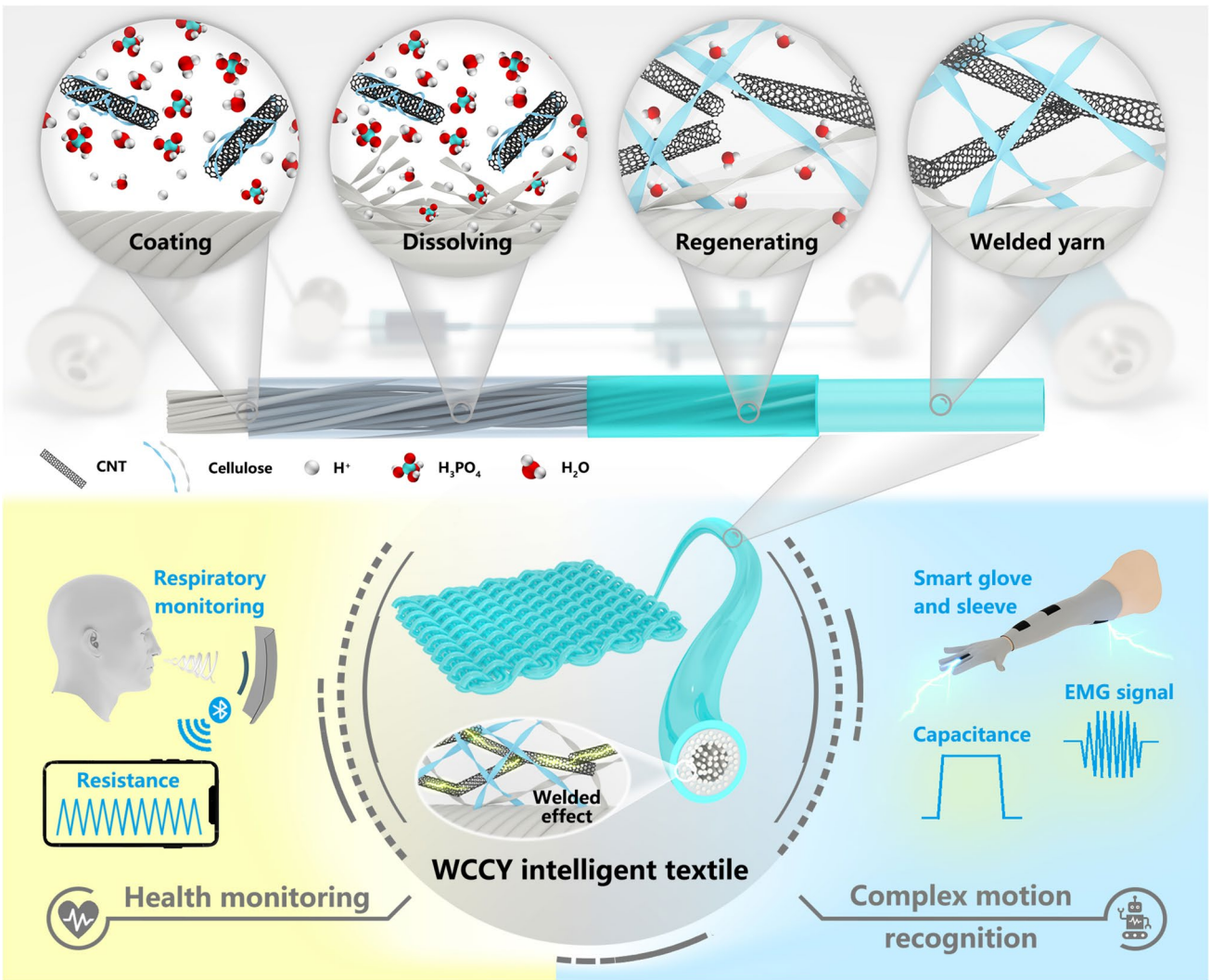


Fig. 1 Schematic illustration depicting the preparation mechanism and application scenarios of the WCCY integrated textiles

of WCCY-based textiles for next-generation health monitoring and human–machine interfaces.

2 Experimental Section

2.1 Materials

Aqueous phosphoric acid (85 wt%) was purchased from Shanghai Titan Scientific Co., Ltd. Copper (II)–ethylenediamine complex (1 M solution in water) was purchased from Shanghai J&K Chemical Technology Co., Ltd. Carbon nanotube (CNT) was purchased from Nanocyl S.A., Belgium. Microcrystalline cellulose powder was purchased from Shanghai Macklin Biochemical Co., Ltd. The organic solvents, including ethanol, acetone, and formic acid, were purchased from Shanghai Titan Scientific Co., Ltd. The inorganic salts, containing LiBr, LiCl, $MgCl_2$, K_2CO_3, NaBr, NaCl, KCl, and $CuSO_4$, were purchased from Sinopharm Chemical Reagent Co., Ltd. Cotton yarn was purchased from a local dealer and used as the raw materials. It is made from 100 % cotton fiber spun into yarn by ring spinning and bleached. The linear density is about 34 ± 0.65 tex with the average diameter of 250 ± 5.56 μm. The applied twist is (80 ± 6.22)/10 cm. The average number of cotton fibers in the cross-section of the yarn is about 160 ± 20.85. The composition and structure of the cotton yarn have been characterized, confirming its composition as cellulose. The degree of polymerization (DP) of the cotton yarn was 2027 ± 6.96.

2.2 Fabrication of All-Cellulose Welded Yarn

The pristine cotton yarns were air-dried at 60 °C for 24 h. The dry cotton yarns were passed through a treatment bath containing 85% aqueous phosphoric acid at certain temperature (contact time was controlled at 2 min), then wound in a homemade bobbin and left to stand for 30 min at certain temperature. The temperature of the aqueous phosphoric acid solution was defined as the solvent infiltration temperature and controlled at 25 °C or –18 °C; the ambient temperature during standing dissolution was also controlled at 25 °C or –18 °C (In the following section, room temperature, RT, was defined as 25 °C and subzero temperature, ST, was defined as –18 °C). The treated yarns were immersed in a deionized water coagulation bath until it became neutral, where the phosphoric acid molecules are replaced by coagulation solvents to fully regenerate the dissolved cellulose fraction. Finally, the yarns were air-dried thoroughly at 60 °C to produce all-cellulose welded yarns.

2.3 Preparation of Cellulose/CNT Welding Dope

CNTs and 85% aqueous phosphoric acid were mixed and then sonicated at 300 W for 30 min to obtain a CNT slurry. According to the manufacturer, the CNT were multi-walled carbon nanotubes (MWNTs), with average diameter and length of 9.5 nm and 1.5 μm, respectively. The CNT slurry and microcrystalline cellulose (MCC) were mixed by mechanical stirring at 10,000 r min^{-1} for 10 min using a disperser (Ultra-Turrax, T18, IKA). Both the sonication and stirring steps were carried out in an ice bath to prevent overheating. The resulting mixture was then centrifuged at 10,000 r min^{-1} for 10 min to remove air bubbles, yielding the functional welding dope.

2.4 Fabrication of WCCYs

The pristine cotton yarns were air-dried at 60 °C for 24 h. As shown in Fig. 2a, the dried yarns were brought into full contact with the functional welding dope via a syringe, and a uniform adhesive layer was formed on the yarns under the shearing force. A 19G-needle, serving as the outlet of the dispensing container controls, controlled the amount of applied dope. After coating, the coated yarns were wound onto a homemade bobbin and treated at –18 °C for 30 min. During the subsequent coagulation step, the phosphoric acid was displaced by deionized water, causing the dissolved cellulose to reassemble and entangle with the CNT networks. Finally, the coated yarns were thoroughly air-dried at 60 °C to yield welded cellulose/CNT yarns.

2.5 Washability Measurement

Nine sets of 200 cm long WCCYs were loosely sewn onto a mesh to prevent tangling during washing. The samples were placed in a beaker containing either deionized water or a soap solution and stirred at 500 r min^{-1}, allowing the mesh and yarns to move and bend freely. The soap solution was a standard textile detergent. Six sets of yarns were washed

© The authors https://doi.org/10.1007/s40820-026-02357-8

for 5 h at each of the following temperatures: 30, 40, 50, 60, 70, and 80 °C. The remaining three sets were washed at 30 °C for 10, 15, and 20 h, respectively. After washing, each set was rinsed with deionized water and air-dried at room temperature for at least 12 h. At least 10 sections of 1–2 cm long yarns were cut from each set for measurement and comparison.

2.6 Characterization

The structure of the cellulose–CNT hybrid was analyzed using transmission electron microscopy (TEM, JEM-2100, JEOL). The TEM samples were prepared by dropping regenerated water-based diluted cellulose–CNT hybrid suspension on a copper grid with carbon film. The Raman spectra were recorded with a Laser Confocal Raman Spectroscope (DXR2xi with 532 nm laser, Thermo Fisher Scientific). Thermogravimetric analysis (TGA, TG209F3, Netzsch) was used to confirm the CNT contents in cellulose/CNT composite via the heating rate of 10 °C min^{-1} in a nitrogen atmosphere. Rheological tests for functional welding dopes were carried out on a rheometer (HAAKE MARS 60, Thermo Fisher Scientific) at 25 °C with a 1 mm parallel steel plate (25 mm). The morphology and structure of cotton yarn, welded yarn, and WCCYs were analyzed using scanning electron microscopy (SEM, TM-3030, Hitachi) and field-emission scanning electron microscope (FESEM, Regulus8230). The cross-sections of yarns were obtained by submerging the yarns in liquid nitrogen and then manually breaking the frozen yarns. The weight of yarn was measured using a scale (ME204E, Mettler Toledo) before and after functional welding to determine the CNT loading. The masses were averaged from three sections of WCCYs with a length of 100 cm. The results are presented in Table S2. The yarn samples were fully dried at 120 °C to constant weight. Mechanical properties of cotton yarn, welded yarn, and WCCYs were performed on an electronic single yarn strength testing machine (YG020B, Changzhou Bels Instrument Co. Ltd.) with 60 %RH at 25 °C and 200 mm min^{-1} stretching velocity. Yarn diameter was determined by the average value of thirty measurements along the yarn length using an optical microscope (OM, Eclipse E100, Nikon). The electrical resistance of WCCY was measured using an LCR meter (TH2832, Tonghui) with a customized LabView program at an AC voltage of 500 mV and a sweeping frequency of 1 kHz by repeating the test in at least ten different positions with 60 %RH at 25 °C. The conductivity of WCCY was calculated as follows:

$$\sigma = \frac{1}{S \cdot R} \tag{1}$$

σ is the conductivity of WCCY, R is resistance obtained in the LCR meter, and l and S correspond to the length and cross-sectional area of measured yarn, respectively.

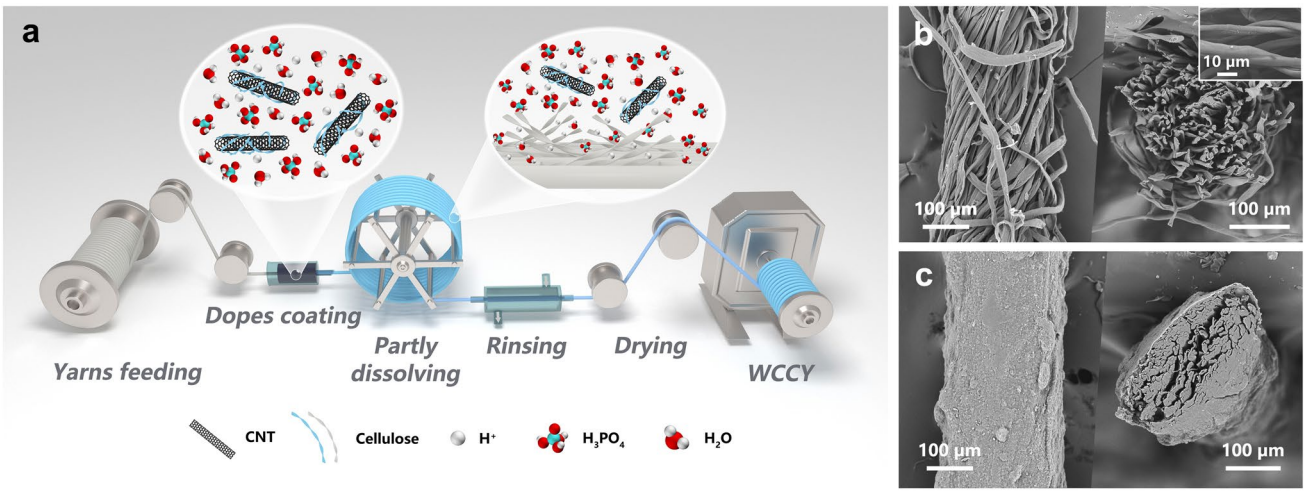


Fig. 2 Preparation and properties of carbon nanotube functionalized welded cellulose yarn. **a** Schematic depicting the preparation of WCCY. SEM images of **b** pristine cotton yarn and **c** WCCY

3 Results and Discussion

3.1 Welding of Cotton Yarns

Figure 2a schematically illustrates the continuous fabrication process of WCCY. As shown, pristine cotton yarns are drawn through a syringe-based coating system containing the CNT-MCC functional welding dope. Under controlled shear forces, the dope forms a uniform, conformal coating layer on the yarn surface (infiltration phase). After coating, the yarns were wound onto a homemade bobbin and subjected to a controlled partial dissolution step at –18 °C for 30 min (dissolution phase). Subsequently, the yarns are immersed in a deionized water coagulation bath, where phosphoric acid is gradually displaced, triggering the regeneration of cellulose chains, which reassemble and entangle with the CNT network, mechanically locking the CNTs in place. Finally, the functionalized yarns are thoroughly air-dried at 60 °C to yield the final WCCYs with integrated core–sheath architecture.

The pristine cotton yarns consisted of twisted cotton fibers with a coarse surface structure (Fig. 2b), facilitating the adhesion and penetration of the welding dopes. During the welding process, aqueous phosphoric acid would partially dissolve the cellulose on surface of yarns, and the loosened cellulose chains would entangle with dissolved MCC in the dope. Subsequently, when phosphoric acid was replaced with coagulation solvent (deionized water), the entanglement was preserved as dissolved cellulose reassembled to form a sheath layer around the original yarn. The diameter of the yarns was barely changed by the welding process, while the density increased noticeably as internal pores were filled with solidified dope (Fig. 2c). The entangled regenerated cellulose (RC) acts as glue to ensure excellent fastness of the CNT decoration.

Before advancing to functionalize welding, we systematically optimized and characterized the continuous fiber welding process in pure phosphoric acid under filler-free conditions, thereby establishing a well-defined process baseline essential for the controlled, in situ integration of CNTs in subsequent stages.

As shown in Fig. 3a, the solvent welding technique for cellulose yarns is based on the partial etching and dissolution of the cellulose fibers in yarns surface by aqueous phosphoric acid. We should mention that 85 wt% aqueous phosphoric acid is essential, as concentrations below this critical threshold fail to efficiently dissolve the native cotton fibers with high degree of polymerization under mild conditions [28]. The dissolved component, acting as an adhesive, binds the loosely arranged cotton fibers together, thus achieving the self-reinforcing welding effect. This preparation process of welded yarns could be divided into a solvent infiltration phase, a partial dissolution phase, and an entanglement regeneration phase. The depth and uniformity of the welding effect are dependent on the degree of solvent infiltration and dissolution. We identified temperature as critical parameter governing the permeation and controlled dissolution of cellulose in aqueous phosphoric acid. As shown in Figs. 3b, c and S1, at room temperature (RT), the aqueous phosphoric acid exhibits excellent penetration into the cotton yarn structure, leading to extensive welding (Fig. S1a, b). In contrast, at subzero temperature (ST), welding efficiency is significantly reduced, primarily due to restricted solvent penetration limited to the yarn surface, a consequence of increase solvent viscosity at low temperatures (Fig. S1c).

Similarly, the significant impact of temperature in the welding process is clearly reflected in the resulting mechanical properties of the welded yarns. As shown in Fig. 3d, e, if the infiltration and dissolution conducted in both subzero temperature (ST-ST), yielded only a 30.3% enhancement in tensile strength of the yarn, due to limited solvent penetration and superficial welding. In contrast, room temperature treatment (RT-RT) enables deep fiber fusion, resulting in a 93.5% increase in tensile strength of the yarn. But the average degree of polymerization of the cellulose had a remarkable reduction (Fig. S2), indicating excessive cellulose degradation. We found out later that, neither pure RT nor pure ST conditions delivered optimal welding performance. So, we developed a two-stage RT-ST strategy: RT was applied during the infiltration phase to ensure maximal solvent penetration, followed by ST during the dissolution phase to suppress excessive depolymerization of the cellulose. Consequently, the yarns prepared under the RT-ST protocol exhibited the highest tensile strength and optimal welding performance. In addition, the Young's modulus and toughness of the welded yarns were also significantly enhanced (Fig. 3f). Briefly, this temperature-programmed welding technique offers a simple yet highly effective route to improve the mechanical properties of cellulose yarns.

© The authors
https://doi.org/10.1007/s40820-026-02357-8

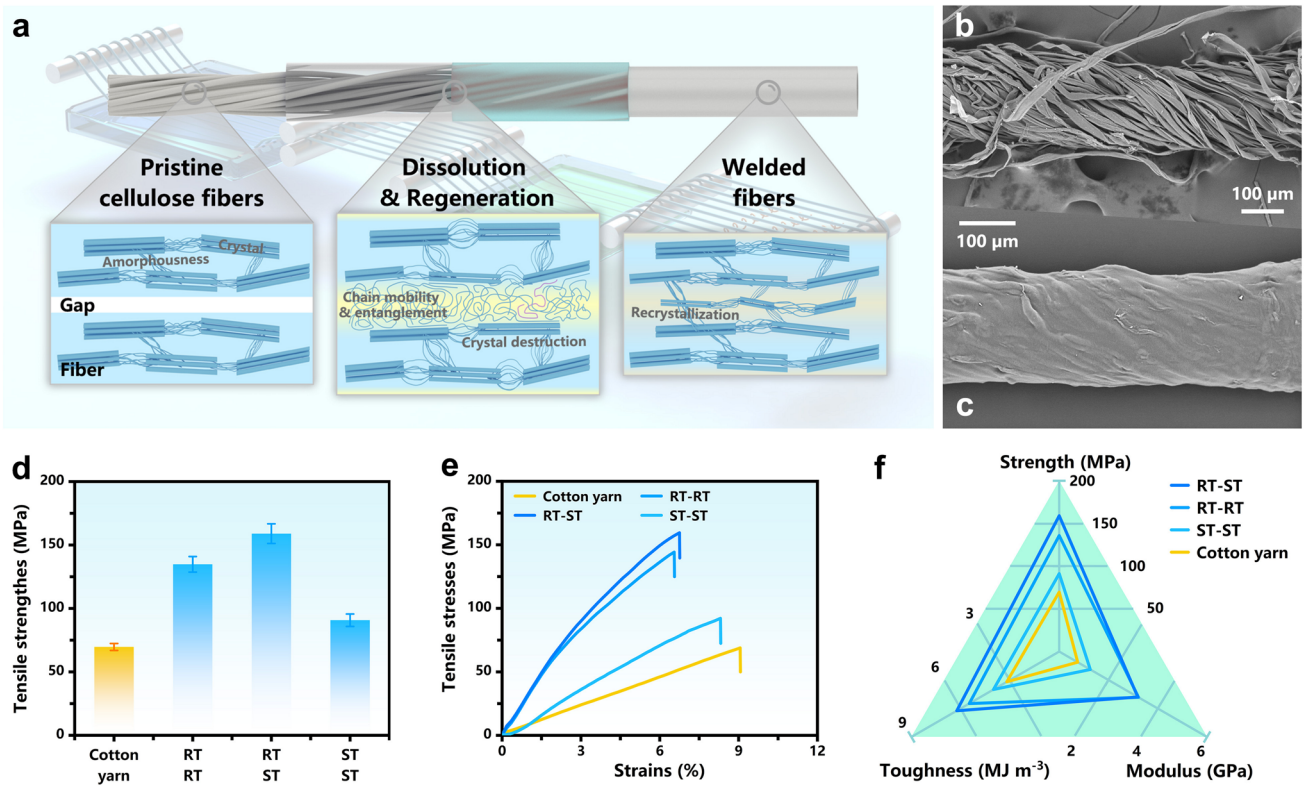


Fig. 3 Fabrication and properties of welded yarn in pure phosphoric acid under filler-free conditions. **a** Schematic depicting the preparation mechanism of all-cellulose welded yarn. Scanning electron microscope (SEM) images of **b** the surface pristine cotton yarn and **c** welded yarn prepared under the RT–ST condition. **d** Tensile strengths, **e** typical tensile stress–strain curves, and **f** mechanical performance comparison of pristine cotton yarn and welded yarns prepared under different process conditions

X-ray diffraction (XRD) analysis revealed that the outer layer of the welded yarn exhibited a significantly increased amorphous fraction of RC compared to the pristine cotton yarn, indicating that the RC phase functions as a natural, in situ formed adhesive that binds adjacent fibers (Fig. S3). Fourier transform infrared spectroscopy confirmed that the characteristic peaks of the welded yarn attributed only to cellulose macromolecules (Fig. S4). Notably, characteristic peaks associated with P-O-C and P-OH groups (at 829 and 927 cm^{-1}), are absent, confirming that cellulose dissolution in aqueous phosphoric acid proceed without derivatization. Hence, welded yarns enabling the retention of the advantages of cellulose on the basis of improved mechanical performances. We believed that the welding technique could serve as a versatile platform for the functionalization of cellulose yarns. By integration functional agents into the welding dope, they can be simultaneously immobilized within the fiber matrix during structural reconstruction, dramatically improving their fastness and mechanical retention.

The initial and challenging step in preparing the self-reinforced conductive welded yarn began with the dispersion of CNTs in the welding dope, which was achieved by the favorable interaction between dissolved MCC and CNT. In deionized water, CNT presented large agglomerates and underwent rapid sinking due to the π–π agglomerate and hydrophobicity of CNT (Fig. 4a(i)). However, the addition of cellulose, MCC, into the CNT/aqueous phosphoric acid slurry facilitated the uniform dispersion of CNT due to the amphiphilicity of dissolved cellulose (Figs. 4a(ii) and S5). Figure 4b shows that uniformly dispersed CNT based on the interaction between cellulose and CNT. The Raman spectra of pure CNT and the CNT/cellulose composites exhibited that the addition of cellulose shifted all three feature peaks toward higher wavenumbers, which was more prominent with increasing content of cellulose (Fig. 4c). The result indicated the non-covalent CH–π interaction between cellulose and CNT, and that interaction enhanced the dispersion of the CNTs.

For better understanding the role played by dissolved cellulose in facilitating the dispersion of CNTs in a polar solvent environment, the system was modeled using molecular dynamic (MD) simulation [30]. Figures 4d and S6a exhibited the interaction process between cellulose and CNT. To quantify the interactions, we calculated the distance between the atoms of cellulose and the surface of CNT based on the atomic coordinates and MATLAB script (Note S1). Remarkably, the evolution diagram of the process (Figs. 4e and S6d) showed that the atoms of cellulose chain IV transferred

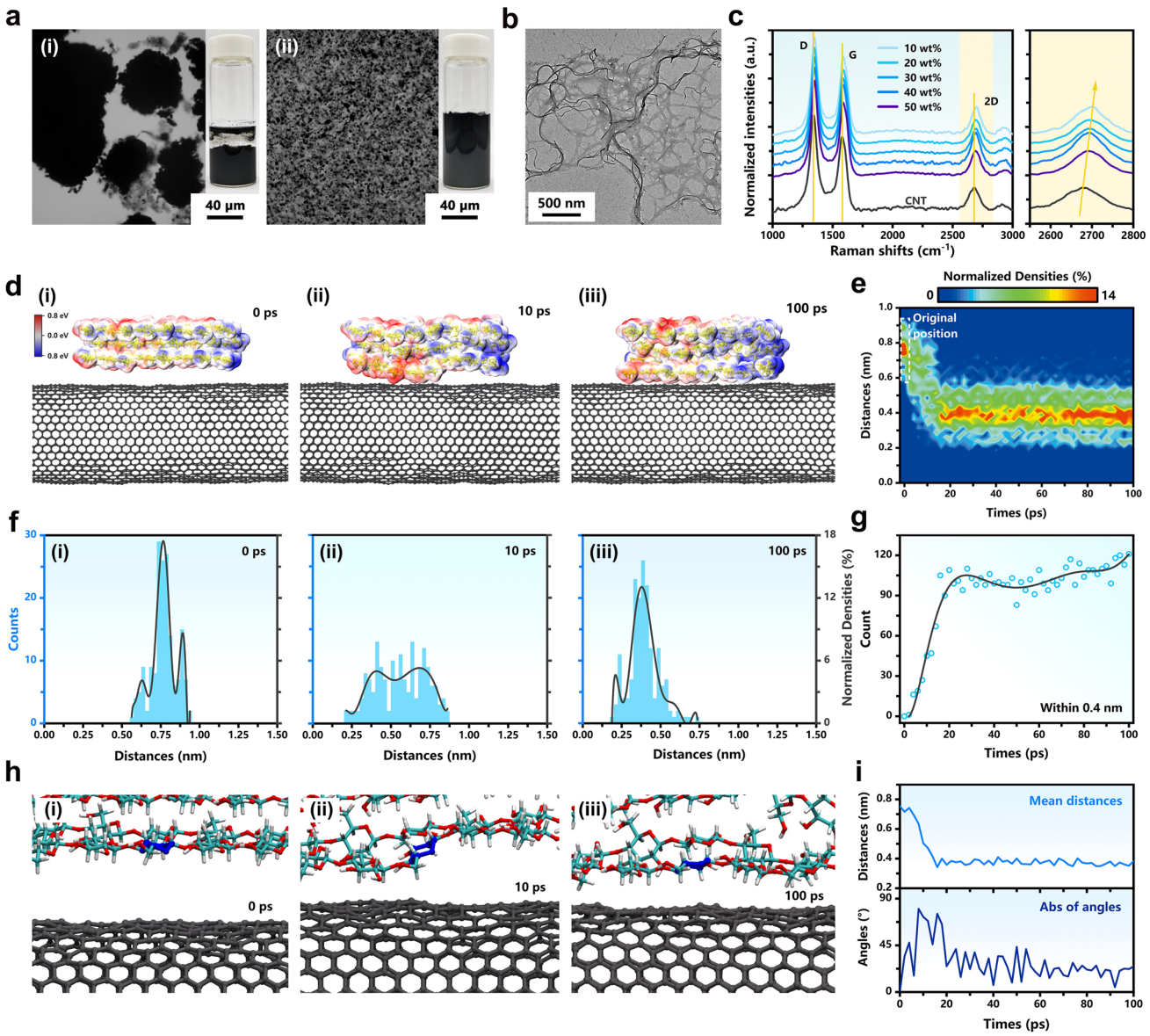


Fig. 4 Dispersion properties of CNTs in welding dopes. **a** Optical microscope images and photographs of the CNT slurry dispersed (i) in water and (ii) in aqueous phosphoric acid with assistance of MCC. **b** TEM image showing uniformly dispersed CNTs. **c** Raman spectrum of MCC/CNT composites with different CNT contents. **d** Frame images and electrostatic potential (ESP) surface of the system at 0, 10, and 100 ps. The solvent molecules of water and phosphoric acid are hidden for the clear schematic diagram. **e** Evolution of normalized densities of the distances between the atoms of cellulose chain IV and the surface of CNT. **f** Statistical histograms and normalized densities of the distances between the atoms of cellulose chain IV and the surface of CNT at 0, 10, and 100 ps. **g** Number of atoms of cellulose chain IV within 0.4 nm from the surface of CNT within 100 ps. **h** Frame images of the pyranose ring at 0, 10, and 100 ps. **i** Distances and line-plane angles between the pyranose ring and the surface of CNT within 100 ps (Colors for the atom scheme: C, gray; O, red; and H, white). The definition of distance and line-plane angle is illustrated in Fig. S7

© The authors
https://doi.org/10.1007/s40820-026-02357-8

to the vicinity of 0.4 nm to form an absorption layer. For analyzing the evolution of the absorption layer, the atomic number of cellulose chain IV within 0.4 nm from the surface of CNT was counted (Figs. 4g and S6e). The atomic count increased significantly around 20 ps and then remain relatively steady, indicating the stability of the adsorption layer. The distance distributions of the initial phase (0 ps), migration phase (10 ps), and stable adsorption phase (100 ps) were plotted separately (Figs. 4f and S6b). Originally, the three peaks of the statistical histogram corresponded to a plane of the pyranose rings and two low-polar planes above and below the pyranose rings. As time went on, the chain IV of cellulose fibril gradually migrated to the surface of CNT so that the peaks tended to flatten out and shifted to the left. When the chain IV was stably adsorbed on the surface of CNT, the three plane peaks reappeared and existed until the end of the simulation.

Cellulose displays hydrophobicity for the upper and lower planes of its pyranose rings and hydrophilicity for polar hydroxyl groups located on the peripheral of the rings [31]. In aqueous phosphoric acid, the pyranose ring tended to be adsorbed on the hydrophobic surface of CNT leading to attenuating the energy of the system. The formation of cellulose–CNT hybrid rendered uniform dispersion of CNT in aqueous phosphoric acid. To further corroborate this adsorption effect, we analyzed the migration evolution process of one pyranose ring in cellulose chain IV (Fig. 4h, i). Due to the initial parallel arrangement, the line-plane angle between the pyranose ring and the center line of CNT is 0°. The increase of angle during the migration process indicated that the cellulose molecular chain undulatingly migrated to the adsorption site. After stable adsorption, the pyranose ring vibrated in a limited range on the surface of CNT and no longer diffused into the solvent. Hence, we inferred that the hydrophobic interactions are essential for the formation and stable existence of the cellulose–CNT hybrid.

The stability and rheological properties of welding dopes are crucial in welding technique. Thermogravimetric analysis (TGA) of the dopes revealed that the content of CNT was almost identical to the theoretically calculated value, demonstrating no destructive effect of phosphoric acid on CNT (Fig. S8a, b). The viscosity of welding dopes at different shear rates manifested their shear thinning behavior, facilitating the penetration of welding dopes into yarns (Fig. S9a). The welding dope exhibited excellent dispersion stability, showing no sedimentation after storage at room temperature for 7 days (Figs. S8c, d, and S9b).

3.2 Electrical Conductivity and Practical Stability of WCCYs

A series of welding dope (Table S2) were used in the continuous fabrication of WCCYs. The welded effect contributed to enhanced mechanical properties of the treated yarns. As shown in Figs. 5a and S10a, the tensile strength of WCCYs with varying CNT loadings was significantly improved across all formulations. The maximum tensile strength, 122.6 ± 5.2 MPa, was achieved at a CNT content of 5.2 wt%, representing a 77.9% increase compared to untreated cotton yarn. At CNT concentrations below 5.2 wt%, the dope was not sticky enough to adhere to the yarn surface, resulting in an uneven coating and reduced performance. Conversely, when the CNT concentration exceeded 5.2 wt%, the increased system viscosity hindered the penetration of aqueous phosphoric acid into the yarn substrate, leading to poor welding performance. In addition, different processing temperature conditions were also compared, and the results were consistent with those of the all-cellulose welded yarns (Fig. S10b).

Using the scalable functional welding technique, hundreds of feet of WCCY can be produced in a single run (Fig. 5b). The treated yarn could also be tied into a knot without breaking, demonstrating excellent flexibility and weavability (Fig. S11). By integrating conventional weaving technologies, conductive fabrics can be readily fabricated from WCCYs (Fig. 5c).

Electrical conductivity is a critical prerequisite for the application in smart wearable electronics. Both the WCCYs and the resulting fabric exhibit good conductivity (Fig. 5d). The conductivity of the WCCYs rose as CNT loading increased (Fig. S10c). Notably, the rate of increase appeared to accelerate beyond a CNT loading of 3.4 wt% (Fig. 5e).

To further elucidate the relationship between microscopic molecular interactions and macroscopic electrical performance, the role of cellulose–CNT adsorption in governing the percolation network was systematically analyzed based on the two-stage linear fitting of conductivity (Fig. 5e). The strong affinity between the amphiphilic cellulose chains and CNT surfaces (validated by MD simulations) critically

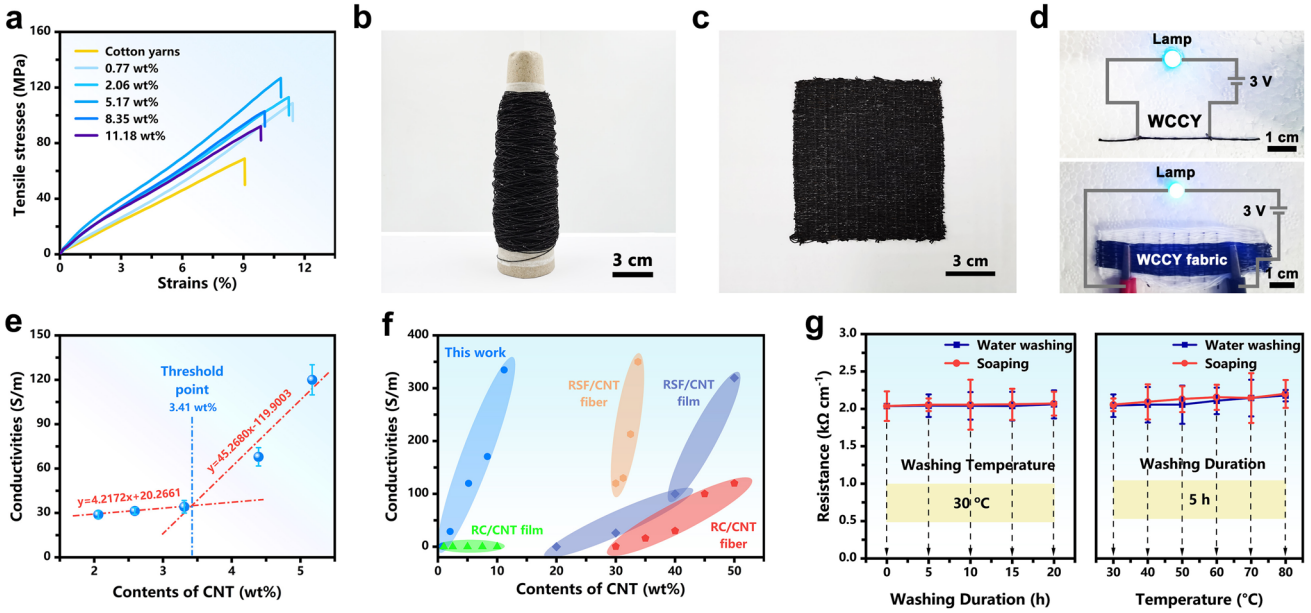


Fig. 5 Properties of carbon nanotube functionalized welded cellulose yarn. **a** Typical tensile stress–strain curves of pristine cotton yarn and WCCY with different CNT loading. Photograph of **b** the collected WCCY on a roll and **c** conductive fabric woven with WCCY. **d** WCCY and its fabric were used as wires to light a lamp under 3 V power supply. **e** Electrical conductivity of WCCY with different CNT loading. **f** Comparison of WCCY to reported biomass-based CNT conductive materials (RC/CNT fiber [32], RC/CNT film [33], regenerated silk fibroin (RSF)/CNT fiber [34], and RSF/CNT film [35]) in conductivities under different contents of CNT. **g** Resistance variations of WCCYs as a function of washing duration (ranging from 0 to 20 h) at a constant washing temperature of 30 °C and as a function of washing temperature (ranging from 30 to 80 °C) at a fixed duration of 5 h by water washing and soaping washing tests of WCCYs with a CNT loading of 5.2 wt%

prevents CNT re-aggregation, ensuring a high degree of exfoliation and an optimized effective aspect ratio during the welding process. Experimentally, the WCCYs exhibit a distinct two-stage electrical percolation behavior divided by a critical threshold point of 3.4 wt%.

When the CNT loading is below the percolation threshold, the linear relationship between electrical conductivity and CNT loading is: $y = 4.2172x + 20.2661$, ($R^2 = 0.9988$). Remarkably, once the CNT loading exceeds the percolation threshold, these discrete pathways instantly interconnect to establish a dense, continuous electrical network. This geometric transition triggers a sharp inflection in electron transport, describe by the linear relationship: $y = 45.2680x - 119.9003$, ($R^2 = 0.9576$). The slope in this post-percolation stage increases by more than tenfold, quantitatively demonstrating that the MD-verified molecular adsorption successfully translates into highly efficient macroscopic electrical connectivity and an optimized, minimized percolation threshold.

It is also worth noting that the WCCYs achieved higher conductivity at relatively lower CNT loadings compared to similar CNT-based conductive biomass composites (Fig. 5f) [32–35]. This enhanced performance, afforded by the functional welding technique, stems from the fact that all conductive CNT fillers were concentrated in the sheath layer of the yarn, maximizing their contribution to electrical conduction.

We employed Raman spectroscopy to analyze the core–sheath architecture of WCCYs. As shown in Fig. S11c, pristine cellulose exhibits a characteristic peak at 383 cm^{-1} compared with its regenerated counterpart. The incorporated CNTs display a characteristic D-band resonance at 1340 cm^{-1} (Fig. 4c). By selectively monitoring the spatial intensity at these specific wavenumbers, 383 and 1340 cm^{-1}, we obtained Raman depth-mapping images of WCCYs, and a clear core–sheath partitioning is revealed. At 383 cm^{-1}, the Raman peak intensity remains highly suppressed at the peripheral surface zone but escalates progressively toward the deeper interior domain (Fig. S11d). This spatial gradient confirms that the outer boundary consists predominantly of fully welded, regenerated amorphous cellulose, leaving the crystalline natural cellulose intact within the interior core. At 1340 cm^{-1}, the surface region exhibits a strong D-band Raman peak intensity from CNTs, while the intensity

© The authors
https://doi.org/10.1007/s40820-026-02357-8

progressively decreases in the deeper region, suggesting that the CNT conductive network is distributed in the outer shell layer of the yarn (Fig. S11e). Taken together, these contrasting spatial profiles deliver unambiguous experimental evidence that the WCCYs possess a well-defined core–sheath architecture, consisting of a highly conductive, structurally integrated regenerated cellulose–CNT sheath seamlessly welded around a mechanically resilient native cellulose core.

In terms of practicality, the washability of wearable electronics is always a primary concern. Hence, we further investigated the washability of WCCYs (with 5.2 wt% CNTs loading) in water and soap solution under different washing temperatures and durations. As shown in Fig. 5g, WCCYs manifested minimal change in electrical resistance after washing for 20 h at 30 °C. The electrical resistance variation, in both water and soap solutions, was less than 2% at 30 °C and less than 7% at 80 °C. In addition, WCCYs with a CNT loading of 3.3 wt% (the percolation threshold) also exhibit excellent washability under various washing conditions, with the increase in electrical resistance remaining below 7% in all cases (Fig. S12a). SEM images illustrated that the CNT functionalized sheath layer was not damaged after washing (Fig. S12b, c).

Leveraging the exceptional dissolving capability of phosphoric acid toward cellulose, alongside the intrinsic amphiphilic nature of cellulose chains, this strategy simultaneously achieves the homogeneous CNT dispersion and robust interfacial welding onto the substrate. Distinct from conventional cellulose dissolution and regeneration strategies, which typically employ dissolved cellulose merely as a passive ex situ coating binder or involve total matrix dissolution for fiber spinning, the molecular-scale welding concept reported herein relies on the controlled, partial, and in situ dissolution of the native yarn substrate. Specifically, the aqueous phosphoric acid selectively unpacks the surface of the yarn, generating dynamic cellulose chains that function as molecular docking sites. During the subsequent in situ regeneration, these liberated substrate chains undergo structural interpenetration and topological entanglement with the MCC chains that disperse the CNTs. Upon hydrogen bond reformation, the CNTs are tightly locked within a seamless, molecularly interwoven gradient interface rather than a simple physical boundary. This mechanism effectively eliminates the severe interfacial mismatch and delamination issues characteristic of conventional top-down blending or physical coating methodologies, thereby affording significantly enhanced anchoring fastness and interfacial robustness.

3.3 Sensors Based on the Swelling–Shrinking Behavior

The conductivity of WCCY, enabled by its embedded conductive CNT network, changes upon exposure to moisture or solvent vapors due to swelling of the cellulose matrix. As shown in Fig. 6a, when WCCY is exposed to protic or polar solvents, solvent molecules diffuse into the amorphous regions of cellulose, disrupting the hydrogen bonding networks. This disruption induces matrix swelling and dislocation of the conductive pathways. Upon solvent evaporation, the interchain hydrogen bonding network of cellulose would reestablish, leading to the recovery of the conductive network. The solvent and moisture-induced reversible swelling of the cellulose matrix thus generates characteristic resistance variations signals. Based on this mechanism, we conclude that the WCCY is suitable for sensing specific solvents and ambient humidity.

The resistance response of the WCCY sensor to various solvents is shown in Fig. 6b. As illustrated, exposure to deionized water and formic acid induced pronounced and prolonged resistance surges, which cause significant matrix swelling. In contrast, acetone produced a small but sharp peak, reflecting its weak interaction with cellulose and high volatility. Ethanol also elicited a weak response, but with a broader peak, indicative of similarly weak cellulose–solvent interactions coupled with lower volatility. These response characteristics showed excellent reproducibility over multiple cycles (Fig. S13). Collectively, the results demonstrate that WCCY holds significant potential as a solvent-responsive sensor.

Using ethanol as an example, we demonstrated that WCCY sensor enables quantitative detection of the target solvent in aqueous solution. Figure 6c shows the resistance variations of the WCCY sensor after transitorily soaking in aqueous ethanol solution. The resistance response curves show three distinctive phases corresponding to rapid swelling, static equilibrium, and evaporation. Higher ethanol concentrations produce weaker and sharper signal curves, owing to ethanol's lower polarity and higher volatility compared to water. The time required to reach equilibrium also varies with ethanol concentration. Molecular dynamic simulations reveal that the diffusion coefficients first decrease and then

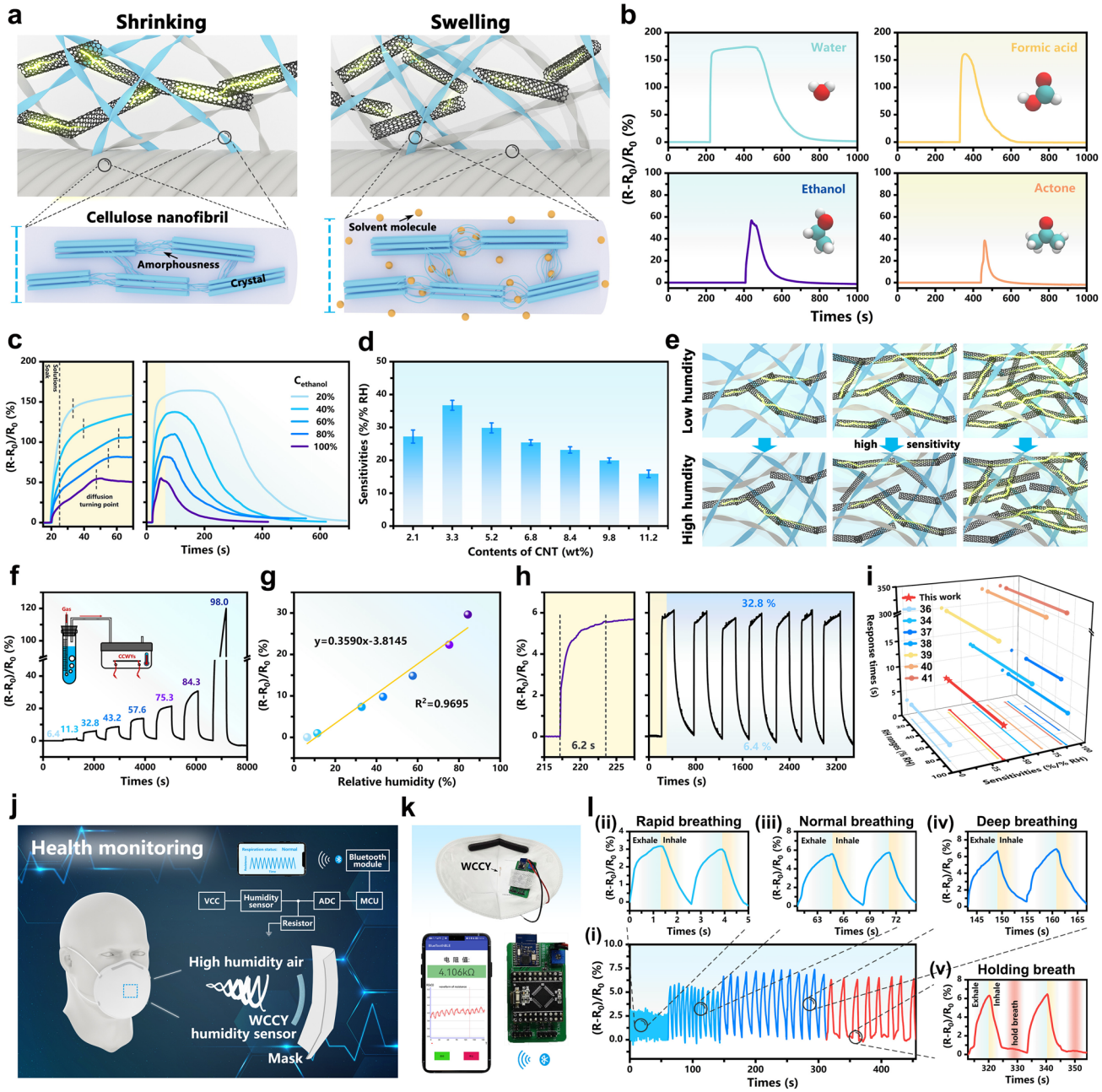


Fig. 6 Sensing performances of WCCY-based resistance sensors. **a** Schematic diagram of the sensing mechanism. **b** Resistance response upon exposure to different solvents (water, formic acid, ethanol, and acetone) and **c** aqueous ethanol. **d** Sensitivities of WCCY humidity sensors as a function of CNT contents. **e** Schematic depiction of the extent of disruption in CNT conductive pathways (with varying densities) caused by swelling of the cellulose network. **f** Real-time response of WCCY humidity sensor at different RH levels from 6.4 to 98.0%. **g** Calibration curve of the WCCY humidity sensor. **h** Dynamic stability and response time of the WCCY humidity sensor under cyclic exposure to 6.4% and 32.8% RH. **i** Performance comparison of the WCCY humidity sensor with representative bio-based humidity sensors in terms of sensitivity, operational RH range, and response time. **j** Schematic illustration of a humidity sensing face mask designed for respiratory monitoring. **k** Optical image of smart mask and its modular units. **l** (i) Real-time electric resistance signals with four distinct respiratory states: (ii) rapid breathing, (iv) normal breathing, (iii) deep breathing, and (v) holding breath (simulating apnea)

© The authors
https://doi.org/10.1007/s40820-026-02357-8

increase with rising ethanol concentration, in good agreement with the experimental results (Fig. S14).

WCCY also exhibits a noticeable change in resistance upon exposure to moisture, making it suitable for sensing relative humidity (RH). The humidity response signal is derived from the relative resistance variations of WCCY measured under different RH conditions. The sensitivity is one of the key performance indicators for characterizing a humidity sensor, and it is quantified as follows:

$$S=\frac{100 \cdot \Delta R}{R_0 \cdot \Delta \%\mathrm{RH}} \quad (2)$$

where S is the ratio of the percentage change in resistance to the percentage change in RH, ΔR is the resistance variation corresponding to RH change (Δ%RH), and R_0 is the initial resistance of the humidity sensor at 6.4 %RH.

The sensitivity of WCCY humidity sensors was evaluated and calculated across a RH range of 6.4–84.3%, using WCCY with varying CNT loadings. As shown in Fig. 6d, the results revealed that optimal sensitivity was achieved at a CNT content of 3.3 wt%, which is close to the electrical percolation threshold. Integrating these findings with the relationship between conductivity and CNT content, we propose a conductive pathway model (Fig. 6e). When CNT content is below the threshold, the conductive pathways are sparse, and localized hygroscopic swelling of the cellulose networks has minimal impact on CNT pathways; when CNT content exceeds the threshold, the dense conductive network is largely resistant to disruption by cellulose swelling. Moreover, higher CNT loadings further reduce this disruption. However, when CNT contents are near the threshold, the cellulose and CNT networks are uniformly interlaced, and hygroscopic swelling of the cellulose significantly perturbs the conductive pathways of the CNTs, leading to maximal sensitivity. Therefore, the WCCY sample containing 3.3 wt% CNT was selected for further studies.

Figure 6f shows that the WCCY sensor responds linearly to changes in RH over the range of 6.4–84.3%. The calibration curve (Fig. 6g) exhibits an optimal sensitivity of 35.90%/%RH. The response at 98%RH deviates slightly from linearity, possibly because the rough surface of the WCCY acts as condensation nuclei for water vapor at such high humidity level, causing enhanced swelling of the cellulose matrix. Moreover, the WCCY-based humidity sensor demonstrates excellent dynamic cyclic stability, with a response time of 6.2 s when transitioning from 6.4 to 32.8%RH (Fig. 6h). Based on the above results, the humidity sensing performances of the WCCY compare favorably with those of the representative bio-based humidity sensors reported in the literature in terms of sensing range, response time, and sensitivity (Fig. 6i), making it promising to be used as humidity sensing materials [34, 36–41].

The integration of portable health monitoring devices with smartphones enables individuals to monitor and manage their health status conveniently, eliminating the need for expensive and bulky medical testing instruments. Building on this concept, we incorporated the highly sensitive and fast-response WCCY humidity sensor into a face mask to create a respiratory monitoring device. We further integrated a signal acquisition unit, a wireless communication module, and a signal data receiving unit (a smartphone) to construct a portable respiratory monitoring system (Fig. 6j, k).

Human exhaled air is typically rich in moisture. Within the confined space of the mask, the alternating cycles of exhalation and inhalation cause corresponding increases and decreases in local humidity. By detecting real-time resistance changes, the system can accurately capture detailed respiratory parameters, including breathing rate, depth, and tidal volume, enabling continuous real-time monitoring of respiratory health. As a proof of concept, a real-time respiratory monitoring test was conducted to record a volunteer's breathing patterns over a 455-second period. Figure 6l shows the signal output under four conditions: normal breathing, deep breathing, rapid breathing, and breath-holding (simulated respiratory arrest). During exhalation, the sensor resistance ascended; during inhalation, the resistance descended. Therefore, each full resistance fluctuation corresponds to one respiratory cycle, allowing respiratory frequency to be calculated from the cycle. For example, deep breathing produced a longer resistance transition time compared to normal or rapid breathing. Moreover, the larger volume of high humidity air, exhaled during deep breathing, generated greater resistance increments. Additionally, this intelligent mask system could recognize abnormal respiratory events, such as respiratory arrest, and triggering an alarm accordingly.

3.4 Capacitive Compressive Strain Textile Sensors

The conductive WCCY can be woven into fabric electrodes for an alternative sensing format. As shown in Fig. 7a, we

constructed a capacitive compressive strain textile sensor (CCSTS) with a sandwich structure by integrating two identical WCCY-based fabric electrodes separated by a 100-μm-thick polydimethylsiloxane (PDMS) dielectric layer. The WCCY-based fabric electrodes featured a plain warp–weft weave with a central rectangular conductive region (12 mm×40 mm) and an insulating border made of pristine cotton yarns.

The electromechanical response of the CCSTS demonstrated its ability to sensitively detect a wide range of compressive strains, from 0 to 40% (Fig. 7b). Notably, the relative capacitance change exhibited a linear relationship with compressive strain in two phases, with fitting slopes of 4.4 and 11.3, respectively. These slopes correspond to the gauge factor (GF) of the CCSTS, an important sensitivity parameter of strain sensors, defined as $\Delta C/\gamma C_0$, where ΔC is the capacitance variation induced by a compressive strain change γ, and C_0 is the initial capacitance of the sensor. The two-stage linear behavior arises from the concavo-convex microstructure of the fabric electrodes, which creates an air gap between the fabric electrode and the PDMS dielectric layer. The capacitance of the plane-parallel capacitor is determined as follows:

$$C = \frac{\varepsilon \cdot S}{4 \cdot \pi \cdot k \cdot d} \quad (3)$$

where ε is the dielectric constant of the dielectric between the two electrodes, S is the overlapping area of two electrodes, and d is the distance between two electrodes. Because the dielectric constant of air is lower than that of PDMS (Table S3), in the low compressive strain phase (0–20%), the air layers constituted a larger fraction of the dielectric layer, leading to a smaller ε; in contrast, under high compressive strain (20–40%), the squeezing effect reduced the air layer volume, resulting in a larger ε and greater capacitance increments (Fig. 7e). The capacitance response of the CCSTS followed changes in compressive strains and remained stable over time (Fig. 7c). Furthermore, the sensor delivered consistent capacitance signals across repeated cycles of varying compressive strain (Fig. 7d). Notably, after 1000 consecutive compression–release cycles at 20% strain, the capacitance response showed no degradation (Fig. 7f), demonstrating excellent long-term cyclic stability. The CCSTS can be sewn into a commercial glove to create a smart glove capable of detecting simple finger flexion (Fig. 7g, h). The relative capacitance change varied proportionally with the degree of finger bending, enabling the system to output distinct signals corresponding to different flexion intensities.

3.5 Bioelectric Detection of CCWY Fabric Electrodes

The system, however, lacked sufficient resolution to distinguish between complex hand gestures, for instance, lightly clenching a fist versus firmly gripping a heavy object. To enhance its discriminative capability, we further broadened the application potential of WCCY-based fabric electrodes by incorporating them into physiological signal detection (Fig. 8a). Based on this integrated multisensory approach, we developed a smart glove and a smart sleeve that combine joint flexion signals with electromyogram (EMG) signals. This hybrid system enables reliable discrimination of complex hand behavioral activities.

The cells and tissues of the human body generate electrical signals that reflect their physiological activity. These bioelectric signals can be captured and recorded using electrodes for applications such as motion monitoring and medical diagnosis [42, 43]. Conventional rigid electrodes typically require conductive gels to reduce the impedance at the skin–electrode interface, but these gels gradually dry out (within 5 days), leading to failure in reliable physiological signal acquisition [44]. In contrast, WCCY fabrics can serve as flexible, fabric-based bioelectric signal acquisition electrodes. Their inherent flexibility, stretchability, and high conductivity enable conformal contact with the skin, significantly lowering the skin–electrode interface impedance (Fig. 8b). As shown in Fig. 8c, WCCY fabric electrodes exhibit lower impedance than commercial gel-based electrodes across a broad alternating current frequency range (10^0–10^4 Hz). To evaluate their performance in EMG, we recorded signals under different muscle activation states of the arm, specifically, the relaxed state, hand-closed state, and clenched-fist state. Figure 8d shows the raw EMG signals and their corresponding magnitude of power (MOP), a metric used to evaluate muscle activating levels, under varying muscle loading conditions. The acquired EMG and electrocardiography (ECG) signals closely resemble those obtained with commercial gel electrodes (Fig. S15). Moreover, WCCY fabric electrodes are also effective for ECG signal acquisition (Fig. 8e). Notably, we evaluated their washability and confirmed that they retain excellent physiological signal recording capabilities even after laundering (Fig. S16).

For human motion recognition, certain behaviors exhibit similar mechanical deformation yet involve significantly different underlying muscle activities. Conventional strain

© The authors
https://doi.org/10.1007/s40820-026-02357-8

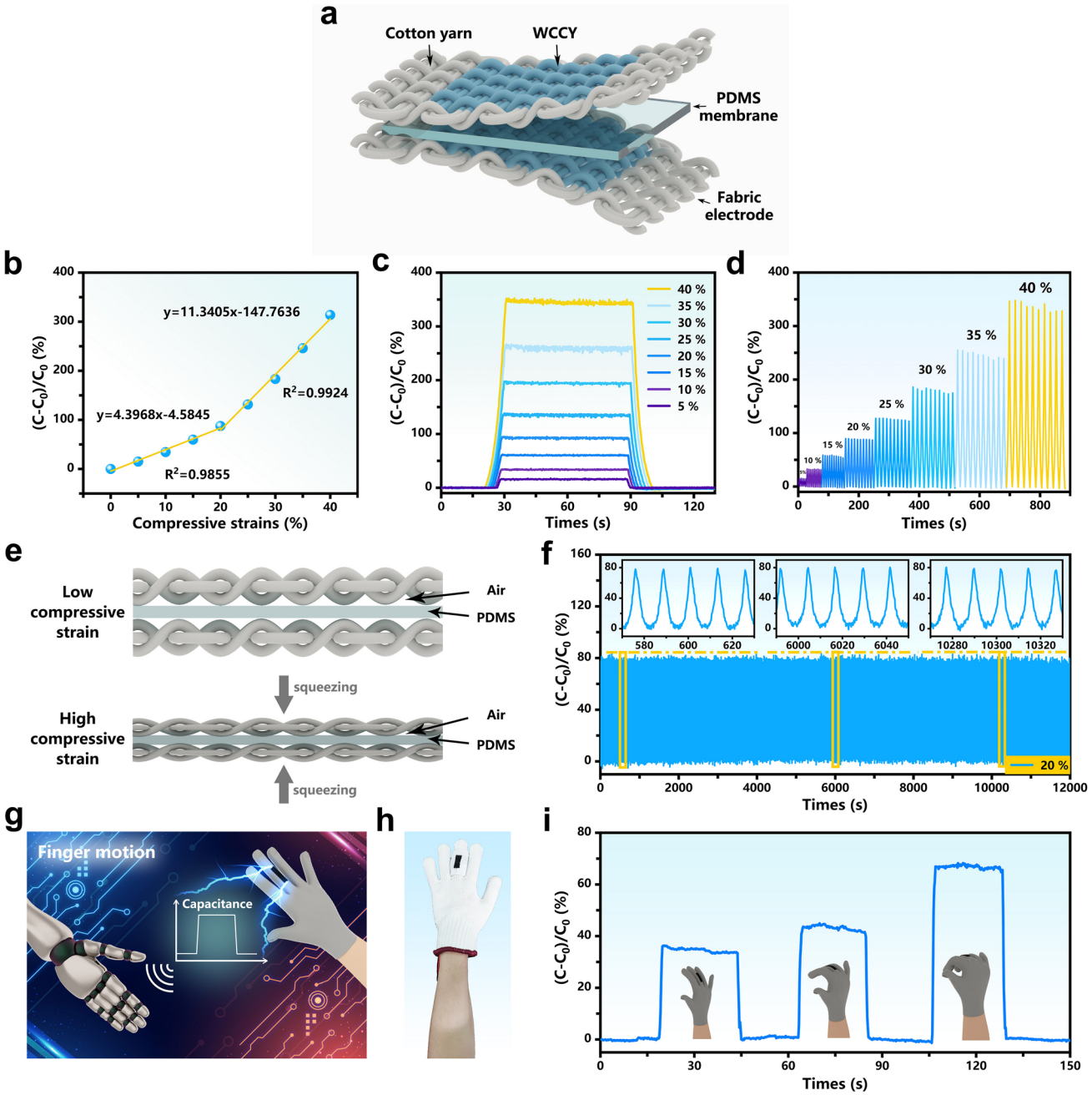


Fig. 7 Sensing and application performances of the capacitive compressive strain textile sensor (CCSTS) based on WCCY fabric electrode. **a** Schematic diagram of the CCSTS (conductive area: 12 mm × 40 mm) assembled by using two WCCY fabric electrodes and a PDMS dielectric layer. **b** Linear correlation of the relative capacitance variations of the sensor with the compressive strain ranging from 0 to 40%. **c** Stability of relative capacitance variations under the compressive strain ranging from 0 to 40%. The hold time is 1 min. **d** Cyclic response of the CCSTS, each cyclic deformation is repeated 10 times. **e** Schematic diagram of CCSTS under different compressive strain conditions, indicating that the proportion of air layer in dielectric layer at high compressive strain is less than at low compressive strain. **f** Measured relative capacitance variations of the sensor during 1000 compressing-releasing cycles under 20% compressive strain, indicating the excellent dynamic cyclic stability. **g** Schematic illustration showing the smart glove based on CCSTS device for detecting finger motions. **h** Optical image of the smart glove. **i** Real-time relative capacitance changes at different finger flexion levels

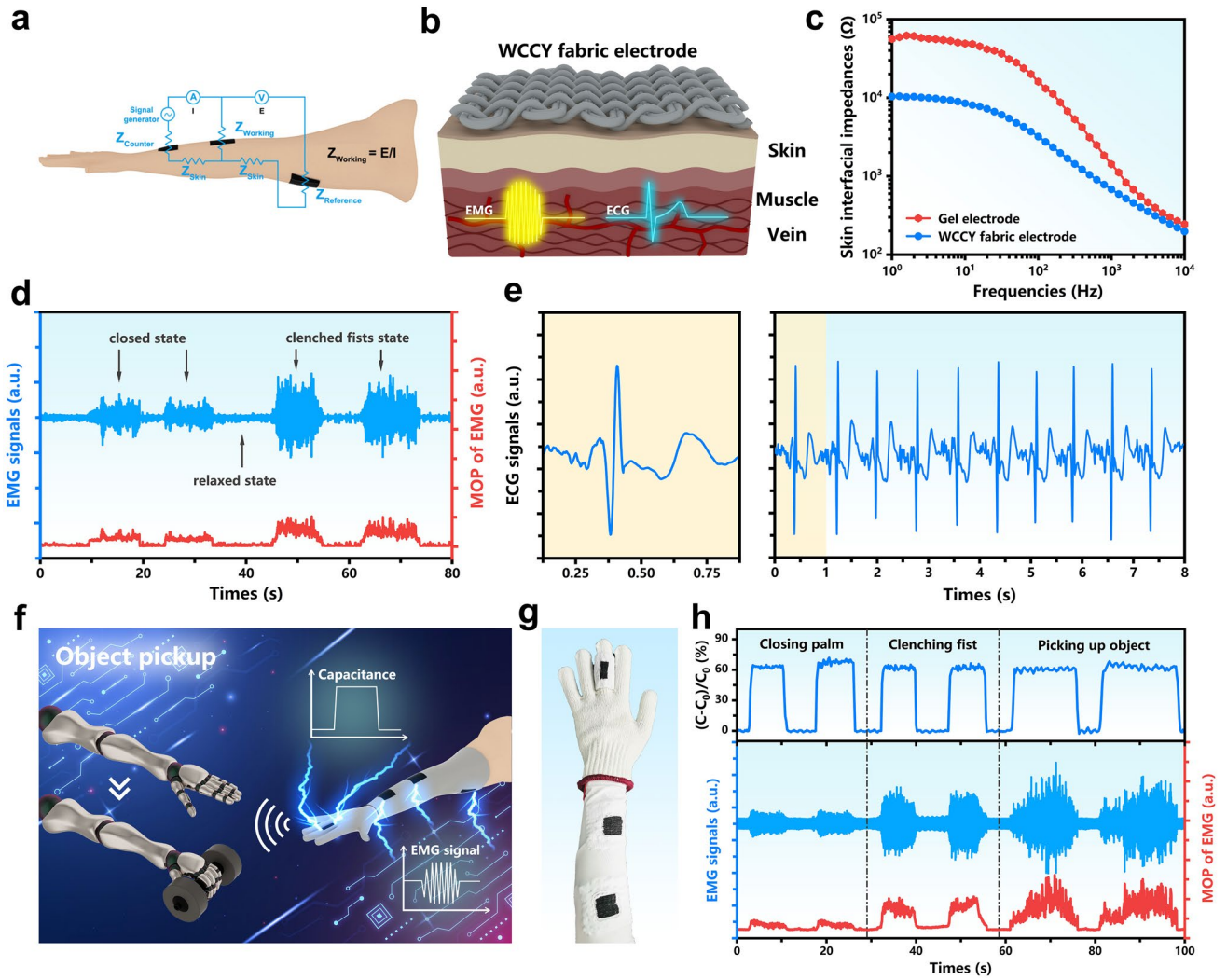


Fig. 8 Electrophysiological sensing performance and application of WCCY fabric electrode. Schematic diagram for **a** measuring impedance between skin and electrode (WCCY fabric electrode or commercial gel electrode) ($Z_{working}$) and **b** WCCY fabric electrodes for collecting electrophysiological signals. **c** Interfacial impedance between electrodes and skin. **d** EMG signals and their magnitude of power (MOP) collected with WCCY fabric electrodes. **e** ECG signals collected with WCCY fabric electrodes. **f** Schematic illustration showing the integrated multisensory textile system based on a compressive–strain sensing glove and an electrophysiological sensing sleeve for recognizing complex hand activities (e.g., object pickup). **g** Optical image of the integrated multisensory textile system. **h** Electric signals collected with an integrated multisensory textile system in different hand activities (e.g., closed state, clenched fists state, and object pickup)

sensors, typically focused on simple motions, lack the capability to distinguish such nuanced actions. To address this limitation, we developed an integrated multisensory system comprising a smart glove and a smart sleeve, capable of recognizing complex hand motions by simultaneously capturing relative capacitance changes and EMG signals (Fig. 8f, g). As a proof of concept, we applied this system to detect three distinct hand behaviors: palm closing, fist clenching, and lifting a heavy object. As shown in Fig. 8h, the capacitance signals from the smart glove revealed similar peak features across all three activities, demonstrating that a strain-based sensing modality alone cannot reliably differentiate complex hand motions. In contrast, EMG signals reflect the degree of muscle activation: Stronger muscle contractions produce larger EMG amplitudes.

Therefore, by fusing data from both the smart glove (capacitive strain sensing) and the smart sleeve (EMG), the three activities were clearly distinguished. For example, palm closing involved minimal muscle loading, resulting in low EMG amplitude and a small MOP. Fist clenching

© The authors
https://doi.org/10.1007/s40820-026-02357-8

engaged muscles more intensely, yielding a strong EMG signal and high MOP. Lifting a heavy object produced a biphasic EMG signal, an initial grasping phase with weak muscle activation (low EMG), followed by a lifting phase with significantly enhanced EMG due to high muscle loading.

These results demonstrate that the integrated multisensory system enables robust discrimination of complex hand behaviors. Furthermore, by combining multiple electrical signal modalities, this platform holds great promise for human–machine interaction, potentially enabling remote control of robotic systems to replicate intricate human actions, thereby advancing the development of next-generation smart wearable devices.

4 Conclusion

In conclusion, we have demonstrated a robust and high-throughput continuous molecular-scale welding technique to transform conventional cellulose yarns into high-performance conductive yarns and extended its applicability to the construction of wearable, integrated multisensory all-textile system. By leveraging a concentrated aqueous phosphoric acid, we achieved the simultaneous dispersion and interfacial anchoring of CNTs within the regenerated cellulose matrix. Molecular dynamics (MD) simulations elucidated the multiple synergistic intermolecular interactions at the cellulose–CNT interface govern the exceptional stability and charge transport efficiency of the system. This scalable manufacturing strategy yielded WCCY with significantly reinforced mechanical integrity, characterized by a 77.9% increase in tensile strength. Notably, the WCCY platform achieved an ultralow electrical percolation threshold and a record-level conductivity of 334.6 S m^{-1} at a low CNT loading of 11.2 wt%, underscoring the superior efficiency of our welding process. Due to the formation of a dense macromolecular entanglement network, the WCCY exhibited remarkable structural and electrical stability even under prolonged exposure to harsh liquid environments (30–80 °C), addressing the long-standing challenge of durability in wearable electronics. Furthermore, the seamless integration of WCCY into a multimodule all-textile smart system enabled the high-fidelity monitoring of environmental stimuli (humidity and organic solvents), biomechanical motions, and physiological electro-signals (ECG/EMG). The successful demonstration of respiratory tracking and fine-grained gesture recognition underscores the potential of WCCY as a versatile building block for sophisticated human–machine interfaces. Given its continuous production capability and the synergistic combination of comfort, durability, and multifunctionality, this WCCY-based textile platform paves a sustainable and effective way for the next generation of intelligent, large-scale wearable electronics.

Acknowledgements X. F and X. S are grateful for the financially supported by the National Natural Science Foundation of China (Nos. 22375038 and 5211101145) and Fundamental Research Funds for the Central Universities (2232026A6, the Interdisciplinary Frontier Innovation Team Development Special Fund of Donghua University). S. Z is grateful for the financial support from the National Science Centre (NCN) in Poland (project no. UMO-2021/40/Q/ST5/00164). The authors thank Mr. Zheng Dong for his assistance with Raman measurements.

Authors Contributions Y. L., X. S., S. Z., and X. F. helped in conceptualization; Y. L., X. S., S. Z., and X. F. helped in methodology; Y. L., C. M., and Y. G. helped in investigation; Y. L. helped in data curation; Y. L., C. M., Y. G., and L. R. helped in formal analysis; C. M. helped in validation; Z. M. and X. F. helped in resources; B. W. worked in project administration; Z. M., B. W., X. S., S. Z., and X. F. worked in supervision; X. S., S. Z., and X. F. helped in funding acquisition; Y. L. and Y. G. helped in visualization; Y. L. contributed to writing—original draft; and Y. L., Y. G., X. S., S. Z., and X. F. contributed to writing—review and editing.

Declarations

Conflict of interest The authors declare no conflict of interest. They have no known competing financial interests or personal relationships that could have appeared to influence the work reported in this paper.

Open Access This article is licensed under a Creative Commons Attribution 4.0 International License, which permits use, sharing, adaptation, distribution and reproduction in any medium or format, as long as you give appropriate credit to the original author(s) and the source, provide a link to the Creative Commons licence, and indicate if changes were made. The images or other third party material in this article are included in the article's Creative Commons licence, unless indicated otherwise in a credit line to the material. If material is not included in the article's Creative Commons licence and your intended use is not permitted by statutory regulation or exceeds the permitted use, you will need to obtain permission directly from the copyright holder. To view a copy of this licence, visit http://creativecommons.org/licenses/by/4.0/.

Supplementary Information The online version contains supplementary material available at https://doi.org/10.1007/s40820-026-02357-8.

References

1. D. Zhao, Y. Zhu, W. Cheng, W. Chen, Y. Wu et al., Cellulose-based flexible functional materials for emerging intelligent electronics. Adv. Mater. **33**(28), 2000619 (2021). https://doi.org/10.1002/adma.202000619
2. L. Lan, J. Ping, J. Xiong, Y. Ying, Sustainable natural bio-origin materials for future flexible devices. Adv. Sci. **9**(15), 2200560 (2022). https://doi.org/10.1002/advs.202200560
3. H. Yin, Y. Li, Z. Tian, Q. Li, C. Jiang et al., Ultra-high sensitivity anisotropic piezoelectric sensors for structural health monitoring and robotic perception. Nano-Micro Lett. **17**(1), 42 (2024). https://doi.org/10.1007/s40820-024-01539-6
4. Y. Sun, W. He, C. Jiang, J. Li, J. Liu et al., Wearable biodevices based on two-dimensional materials: from flexible sensors to smart integrated systems. Nano-Micro Lett. **17**(1), 109 (2025). https://doi.org/10.1007/s40820-024-01597-w
5. H. Wang, Y. Zhang, X. Liang, Y. Zhang, Smart fibers and textiles for personal health management. ACS Nano **15**(8), 12497–12508 (2021). https://doi.org/10.1021/acsnano.1c06230
6. W. Weng, P. Chen, S. He, X. Sun, H. Peng, Smart electronic textiles. Angew. Chem. Int. Ed. **55**(21), 6140–6169 (2016). https://doi.org/10.1002/anie.201507333
7. C. Ye, J. Ren, Y. Wang, W. Zhang, C. Qian et al., Design and fabrication of silk templated electronic yarns and applications in multifunctional textiles. Matter **1**(5), 1411–1425 (2019). https://doi.org/10.1016/j.matt.2019.07.016
8. S. Uzun, M. Schelling, K. Hantanasirisakul, T.S. Mathis, R. Askeland et al., Additive-free aqueous MXene inks for thermal inkjet printing on textiles. Small **17**, 2006376 (2021). https://doi.org/10.1002/smll.202006376
9. D. Zhang, R. Yin, Y. Zheng, Q. Li, H. Liu et al., Multifunctional MXene/CNTs based flexible electronic textile with excellent strain sensing, electromagnetic interference shielding and Joule heating performances. Chem. Eng. J. **438**, 135587 (2022). https://doi.org/10.1016/j.cej.2022.135587
10. F. Guan, Y. Xie, H. Wu, Y. Meng, Y. Shi et al., Silver nanowire–bacterial cellulose composite fiber-based sensor for highly sensitive detection of pressure and proximity. ACS Nano **14**(11), 15428–15439 (2020). https://doi.org/10.1021/acsnano.0c06063
11. C. Cao, Z. Lin, X. Liu, Y. Jia, E. Saiz et al., Strong reduced graphene oxide coated *Bombyx mori* silk. Adv. Funct. Mater. **31**(34), 2102923 (2021). https://doi.org/10.1002/adfm.202102923
12. S. Uzun, S. Seyedin, A.L. Stoltzfus, A.S. Levitt, M. Alhabeb et al., Knittable and washable multifunctional MXene-coated cellulose yarns. Adv. Funct. Mater. **29**(45), 1905015 (2019). https://doi.org/10.1002/adfm.201905015
13. K. Jost, D.P. Durkin, L.M. Haverhals, E.K. Brown, M. Langenstein et al., Natural fiber welded electrode yarns for knittable textile supercapacitors. Adv. Energy Mater. **5**(4), 1401286 (2015). https://doi.org/10.1002/aenm.201401286
14. S. Hu, J. Han, Z. Shi, K. Chen, N. Xu et al., Biodegradable, super-strong, and conductive cellulose macrofibers for fabric-based triboelectric nanogenerator. Nano-Micro Lett. **14**(1), 115 (2022). https://doi.org/10.1007/s40820-022-00858-w
15. D. Jang, K.T. Park, S.-S. Lee, H. Kim, Highly stretchable three-dimensional thermoelectric fabrics exploiting woven structure deformability and passivation-induced fiber elasticity. Nano Energy **97**, 107143 (2022). https://doi.org/10.1016/j.nanoen.2022.107143
16. L. Wang, J. Lu, Q. Li, L. Li, E. He et al., A core–sheath sensing yarn-based electrochemical fabric system for powerful sweat capture and stable sensing. Adv. Funct. Mater. **32**(23), 2200922 (2022). https://doi.org/10.1002/adfm.202200922
17. Q. Liang, D. Zhang, Y. Wu, S. Chen, Z. Han et al., Self-stretchable fiber liquid sensors made with bacterial cellulose/carbon nanotubes for smart diapers. ACS Appl. Mater. Interfaces **14**(18), 21319–21329 (2022). https://doi.org/10.1021/acsami.2c00960
18. C. Zhu, R. Li, X. Chen, E. Chalmers, X. Liu et al., Ultraelastic yarns from curcumin-assisted ELD toward wearable human–machine interface textiles. Adv. Sci. **7**(23), 2002009 (2020). https://doi.org/10.1002/advs.202002009
19. S. Afroj, N. Karim, Z. Wang, S. Tan, P. He et al., Engineering graphene flakes for wearable textile sensors *via* highly scalable and ultrafast yarn dyeing technique. ACS Nano **13**(4), 3847–3857 (2019). https://doi.org/10.1021/acsnano.9b00319
20. R.M.A.P. Lima, J.J. Alcaraz-Espinoza, F.A.G. da Silva Jr, H.P. de Oliveira, Multifunctional wearable electronic textiles using cotton fibers with polypyrrole and carbon nanotubes. ACS Appl. Mater. Interfaces 10(16), 13783–13795 (2018).https://doi.org/10.1021/acsami.8b04695
21. S.Y. Cho, H. Yu, J. Choi, H. Kang, S. Park et al., Continuous meter-scale synthesis of weavable tunicate cellulose/carbon nanotube fibers for high-performance wearable sensors. ACS Nano **13**(8), 9332–9341 (2019). https://doi.org/10.1021/acsnano.9b03971
22. C. Wang, K. Xia, H. Wang, X. Liang, Z. Yin et al., Advanced carbon for flexible and wearable electronics. Adv. Mater. **31**(9), 1801072 (2019). https://doi.org/10.1002/adma.201801072
23. T. Lei, L.-L. Shao, Y.-Q. Zheng, G. Pitner, G. Fang et al., Low-voltage high-performance flexible digital and analog circuits based on ultrahigh-purity semiconducting carbon nanotubes. Nat. Commun. **10**(1), 2161 (2019). https://doi.org/10.1038/s41467-019-10145-9
24. Y. Gao, F. Guo, P. Cao, J. Liu, D. Li et al., Winding-locked carbon nanotubes/polymer nanofibers helical yarn for ultrastretchable conductor and strain sensor. ACS Nano **14**(3), 3442–3450 (2020). https://doi.org/10.1021/acsnano.9b09533
25. H. Souri, D. Bhattacharyya, Wearable strain sensors based on electrically conductive natural fiber yarns. Mater. Des. **154**, 217–227 (2018). https://doi.org/10.1016/j.matdes.2018.05.040
26. Y. Huang, S.V. Kershaw, Z. Wang, Z. Pei, J. Liu et al., Highly integrated supercapacitor-sensor systems *via* material and geometry design. Small **12**(25), 3393–3399 (2016). https://doi.org/10.1002/smll.201601041

© The authors https://doi.org/10.1007/s40820-026-02357-8

27. Y. Wang, C. Yang, Z. Xin, Y. Luo, B. Wang et al., Poly(lactic acid)/carbon nanotube composites with enhanced electrical conductivity *via* a two-step dispersion strategy. Compos. Commun. **30**, 101087 (2022). https://doi.org/10.1016/j.coco.2022.101087
28. H. Su, B. Wang, Z. Sun, S. Wang, X. Feng et al., High-tensile regenerated cellulose films enabled by unexpected enhancement of cellulose dissolution in cryogenic aqueous phosphoric acid. Carbohydr. Polym. **277**, 118878 (2022). https://doi.org/10.1016/j.carbpol.2021.118878
29. Z. Dong, Y. Luo, L. Zhao, B. Wang, Z. Mao et al., All-cellulose composite yarn *via* welding engineering. Carbohydr. Polym. **343**, 122462 (2024). https://doi.org/10.1016/j.carbpol.2024.122462
30. X. Liang, H. Li, J. Dou, Q. Wang, W. He et al., Stable and biocompatible carbon nanotube ink mediated by silk protein for printed electronics. Adv. Mater. **32**(31), 2000165 (2020). https://doi.org/10.1002/adma.202000165
31. D. Klemm, B. Heublein, H.P. Fink, A. Bohn, Cellulose: fascinating biopolymer and sustainable raw material. Angew. Chem. Int. Ed. **44**(22), 3358–3393 (2005). https://doi.org/10.1002/anie.200460587
32. J. Chen, Y. Li, Y. Zhang, D. Ye, C. Lei, K. Wu, Q. Fu, Knittable composite fiber allows constant and tremendous self-powering based on the transpiration-driven electrokinetic effect. Adv. Funct. Mater. **32**(30), 2203666 (2022). https://doi.org/10.1002/adfm.202203666
33. Y. Xie, H. Xu, X. He, Y. Hu, E. Zhu et al., Flexible electronic skin sensor based on regenerated cellulose/carbon nanotube composite films. Cellulose **27**(17), 10199–10211 (2020). https://doi.org/10.1007/s10570-020-03496-w
34. L. Ma, Q. Liu, R. Wu, Z. Meng, A. Patil et al., From molecular reconstruction of mesoscopic functional conductive silk fibrous materials to remote respiration monitoring. Small **16**(26), 2000203 (2020). https://doi.org/10.1002/smll.202000203
35. X. Dong, Q. Liu, S. Liu, R. Wu, L. Ma, Silk fibroin based conductive film for multifunctional sensing and energy harvesting. Adv. Fiber Mater. **4**(4), 885–893 (2022). https://doi.org/10.1007/s42765-022-00152-9
36. Q. Wang, S. Ling, X. Liang, H. Wang, H. Wang et al., Self-healable multifunctional electronic tattoos based on silk and graphene. Adv. Funct. Mater. **29**(16), 1808695 (2019). https://doi.org/10.1002/adfm.201808695
37. S. Kotresh, Y.T. Ravikiran, H.G. Raj Prakash, C.V.V. Ramana, S.C. Vijayakumari et al., Humidity sensing performance of spin coated polyaniline–carboxymethyl cellulose composite at room temperature. Cellulose **23**(5), 3177–3186 (2016). https://doi.org/10.1007/s10570-016-1035-6
38. Y. Wang, L. Zhang, J. Zhou, A. Lu, Flexible and transparent cellulose-based ionic film as a humidity sensor. ACS Appl. Mater. Interfaces **12**(6), 7631–7638 (2020). https://doi.org/10.1021/acsami.9b22754
39. H. Zhao, T. Zhang, R. Qi, J. Dai, S. Liu et al., Drawn on paper: a reproducible humidity sensitive device by handwriting. ACS Appl. Mater. Interfaces **9**(33), 28002–28009 (2017). https://doi.org/10.1021/acsami.7b05181
40. P. Zhu, Y. Liu, Z. Fang, Y. Kuang, Y. Zhang et al., Flexible and highly sensitive humidity sensor based on cellulose nanofibers and carbon nanotube composite film. Langmuir **35**(14), 4834–4842 (2019). https://doi.org/10.1021/acs.langmuir.8b04259
41. P. Zhu, Y. Kuang, Y. Wei, F. Li, H. Ou et al., Electrostatic self-assembly enabled flexible paper-based humidity sensor with high sensitivity and superior durability. Chem. Eng. J. **404**, 127105 (2021). https://doi.org/10.1016/j.cej.2020.127105
42. H. Lee, S. Lee, W. Lee, T. Yokota, K. Fukuda et al., Ultrathin organic electrochemical transistor with nonvolatile and thin gel electrolyte for long-term electrophysiological monitoring. Adv. Funct. Mater. **29**(48), 1906982 (2019). https://doi.org/10.1002/adfm.201906982
43. S. Zheng, W. Li, Y. Ren, Z. Liu, X. Zou et al., Moisture-wicking, breathable, and intrinsically antibacterial electronic skin based on dual-gradient poly(ionic liquid) nanofiber membranes. Adv. Mater. **34**(4), 2106570 (2022). https://doi.org/10.1002/adma.202106570
44. L.W. Taylor, S.M. Williams, J.S. Yan, O.S. Dewey, F. Vitale et al., Washable, sewable, all-carbon electrodes and signal wires for electronic clothing. Nano Lett. **21**(17), 7093–7099 (2021). https://doi.org/10.1021/acs.nanolett.1c01039

Publisher's Note Springer Nature remains neutral with regard to jurisdictional claims in published maps and institutional affiliations.